INFN/AExxx, LAL-xxx, SLAC-R-xxx

Super*B* Detector Technical Design Report

Abstract

This report describes the technical design detector for Super*B*.

Contents

1 Introduction **1**
- 1.1 The Physics Motivation . . . 1
- 1.2 The Super*B* Project Elements . . . 1
- 1.3 The Detector Technical Design Report . . . 2

2 Accelerator Overview **7**

3 Detector Overview **9**
- 3.1 Physics Performance . . . 9
- 3.2 Challenges on Detector Design . . . 12
- 3.3 Open Issues . . . 14
- 3.4 Detector R&D . . . 14

4 Physics with Super*B* **19**
- 4.1 Introduction . . . 19
- 4.2 B and D decays . . . 19
  - 4.2.1 Rare B decays . . . 19
  - 4.2.2 Rare D decays . . . 21
  - 4.2.3 CKM matrix and unitarity triangle . . . 22
  - 4.2.4 CP violation in B decays . . . 23
  - 4.2.5 CP violation in D decays . . . 23
  - 4.2.6 Other symmetry tests . . . 24
  - 4.2.7 Charm mixing . . . 24
  - 4.2.8 B physics at the $\Upsilon(5S)$ . . . 25
- 4.3 τ physics at Super*B* . . . 26
  - 4.3.1 Lepton flavor violation in τ decay . . . 26
  - 4.3.2 CP violation in τ decay . . . 27
  - 4.3.3 Measurement of the τ $g-2$ and EDM form factors . . . 27
- 4.4 Super*B* Neutral Current Electroweak Physics Programme . . . 28
- 4.5 Exotic Spectroscopy in Super*B* . . . 29
- 4.6 Direct searches . . . 31
- 4.7 Executive Summary . . . 31

5 Machine Detector Interface and Backgrounds **37**
- 5.1 Overview M.Sullivan, M. Boscolo E.Paoloni, - 1 page . . . 37
- 5.2 Backgrounds sources. M.Sullivan, M.Boscolo, E.Paoloni, - 2 pages . . . 37
- 5.3 Radiative Bhabha . . . 37
  - 5.3.1 Simulation tools . . . 37
  - 5.3.2 Losses at the beam-pipe . . . 38
  - 5.3.3 Shield System . . . 39
- 5.4 Pairs Production C.Rimbault - 2 pages . . . 40

5.5 Touscheck bacgkround. M.Boscolo - 2 pages 40
5.6 Beam gas background. M.Boscolo - 2 pages 40
5.7 Synchrotron radiation background. M.Sullivan - 2 pages 40
5.8 SVT background overview 40
5.9 DCH background overview R.Cenci D.Lindemann - 2 pages 43
5.10 FTOF background overview 43
5.11 FDIRC background overview 44
5.11.1 Shielding the FDIRC 44
5.11.2 Background rates in the FDIRC 45
5.11.3 Integrated charges and doses 45
5.12 EMC background overview. S.Germani - 2 pages 45
5.13 IFR background overview V.Santoro - 2 pages 46
5.14 ETD background overview 46
5.15 SVT radiation monitor. A.Di Ciaccio- 3 pages 47
5.16 Quick demounting. M.Sullivan, F.Bosi, E.Paoloni - 4 pages 47

6 Silicon Vertex Tracker **51**
6.1 Overview G.Rizzo - 12 pages 51
6.1.1 SVT and Layer0 51
6.1.2 SVT Requirements 53
6.1.2.1 Resolution 53
6.1.2.2 Acceptance 53
6.1.2.3 Efficiency 55
6.1.2.4 Background & Radiation Tolerance 55
6.1.2.5 Reliability 56
6.1.3 Baseline Detector Concept 56
6.1.3.1 Technology 56
6.1.3.2 Layout 56
6.1.3.3 Electronic Readout 58
6.1.3.4 Module design and Mechanical Support 60
6.1.4 Layer0 Pixel Upgrade 61
6.1.4.1 Motivations 61
6.1.4.2 Technology Options for Layer0 pixel upgrade 62
6.1.4.3 Pixel Module & Material Budget 64
6.1.5 R&D Main Activities 65
6.2 Backgrounds R.Cenci - 4 pages 65
6.2.1 Pair production 66
6.2.2 Radiative Bhabha 66
6.2.3 Touschek 66
6.2.4 Beam Gas 66
6.2.5 Other sources 66
6.3 Detector Performance Studies N.Neri - 6 pages 66
6.3.1 Introduction 66
6.3.2 The SVT layout 66
6.3.3 Impact of Layer0 on detector performance 67
6.3.4 Tracking performance 70
6.3.5 Impact of machine background on tracking performance 70

6.3.6 Sensitivity studies for time-dependent analyses . . . 72
6.3.7 Performance with Layer0 pixel detectors . . . 73
6.3.8 Particle identification with dE/dx . . . 74
6.4 Silicon Sensors L. Bosisio - 8 pages . . . 74
6.4.1 Requirements . . . 75
6.4.2 Sensor design and technology . . . 75
6.4.3 Wafer layout and quantities . . . 78
6.4.4 Prototyping and tests . . . 78
6.4.5 z-side strip connection options . . . 78
6.5 Fanout Circuits L.Vitale - M.Prest2+2 pages . . . 79
6.5.1 Fanouts for layer0 . . . 80
6.5.1.1 Requirements . . . 80
6.5.1.2 Technology . . . 80
6.5.1.3 Design . . . 80
6.5.1.4 Prototyping and tests . . . 80
6.5.2 Fanouts for outer layers . . . 80
6.5.2.1 Requirements . . . 80
6.5.2.2 Material and production technique . . . 80
6.5.2.3 Design . . . 80
6.5.2.4 Tests and prototyping . . . 80
6.6 Electronics Readout 28 pages . . . 82
6.6.1 Readout chips V.Re - 10 . . . 82
6.6.1.1 Electronic Readout for Strip and Striplet Detectors . . . 82
6.6.2 Readout chips requirements . . . 83
6.6.3 Readout Chip Implementation . . . 85
6.6.4 R&D for strip readout chips . . . 86
6.6.5 Hybrid Design M.Citterio - 10 . . . 87
6.6.6 Data Transmission M.Citterio - 10 . . . 87
6.6.7 Power Supply - 2 . . . 87
6.7 Mechanical Support and Assembly S.Bettarini/F.Bosi - 14 pages . . . 87
6.7.1 I.R. Constraint . . . 87
6.7.2 Module Assembly . . . 90
6.7.3 Detector Assembly and Installation . . . 92
6.7.3.1 L1-L5 Half detector assembly . . . 92
6.7.3.2 L0 Half detector assembly . . . 96
6.7.3.3 Mount L0 to Be-pipe and L1-L5 to W conical shielding . . . 96
6.7.3.4 Installation of Complete Assembly into the SuperB Detector . . . 99
6.7.3.5 Quick Demounting . . . 99
6.7.4 Detector Placement and Survey . . . 102
6.7.5 Detector Monitoring . . . 102
6.7.5.1 Position Monitoring System . . . 102
6.7.5.2 Radiation Monitoring: in MDI . . . 103
6.7.6 R&D Program . . . 103
6.7.6.1 Cables . . . 103
6.7.6.2 Hybrid . . . 103
6.7.6.3 Be Beam pipe . . . 103
6.7.6.4 L0 Module . . . 103

6.7.6.5 Inner layer sextant . . . 103
6.7.6.6 Arch modules . . . 103
6.7.6.7 Cones and space frame . . . 103
6.7.6.8 Full-scale model of IR and W Cylinder Shield . . . 103
6.7.6.9 Quick Demounting test . . . 104
6.8 Layer0 Upgrade Options G.Rizzo/L.Ratti - 10 pages . . . 104
6.8.1 Technology options . . . 104
6.8.1.1 Hybrid pixels . . . 104
6.8.1.2 Deep N-well CMOS monolithic sensors . . . 106
6.8.1.3 Monolithic pixels in CMOS quadruple well technology . . . 107
6.8.2 Overview of the R&D activity . . . 107
6.8.2.1 Front-end electronics for hybrid pixels in planar and 3D CMOS technology . . . 107
6.8.2.2 The Apsel DNW MAPS series . . . 109
6.8.2.3 The Apsel4well quadruple well monolithic sensor . . . 112
6.8.3 Radiation tolerance . . . 114
6.9 Services and Utilities - 4 pages . . . 116
6.9.1 Service and Utilities . . . 116
6.9.1.1 Data and control lines . . . 116
6.9.1.2 Power . . . 116
6.9.1.3 Cooling water . . . 116
6.9.1.4 Dry air or nitrogen . . . 117

7 Drift Chamber **123**
7.1 Overview - Finocchiaro, Roney 10 pages . . . 123
7.1.1 Physics Requirements - 3 pages . . . 123
7.1.2 Geometrical Constraints . . . 123
7.1.3 Machine Background Considerations - Cenci 3 pages . . . 123
7.1.4 DCH Design Overview - 2 pages . . . 123
7.1.5 Expected Performance - 2 pages . . . 123
7.2 Design Optimization - Finocchiaro, Hearty, Piccolo, Roney 9 pages . . . 124
7.2.1 Cluster Counting . . . 124
7.2.2 Cell Design and Layer Arrangement . . . 124
7.2.3 Gas Mixture . . . 126
7.2.4 R&D and Prototype Studies . . . 126
7.2.4.1 Prototype 1 . . . 128
7.2.4.2 Prototype 2 . . . 129
7.2.4.3 Single Cell Prototypes . . . 130
7.2.4.4 Aging studies . . . 132
7.2.5 R&D Future Developments . . . 135
7.3 Mechanical Design . . . 135
7.3.1 Endplates . . . 135
7.3.2 Inner cylinder . . . 135
7.3.3 Outer Cylinder . . . 136
7.3.4 Choice of wire and electrostatic stability . . . 136
7.3.5 Feedthrough design . . . 136

7.3.6 Endplate systems . . . 137
7.3.6.1 Electronics enclosures . . . 137
7.3.6.2 Cooling . . . 137
7.3.6.3 Shielding . . . 138
7.3.6.4 Electromechanical boards . . . 138
7.3.7 Stringing . . . 138
7.4 Electronics - Felici, Martin 1 page . . . 138
7.4.1 Design Goals . . . 138
7.4.2 Standard Readout - charge measurements specifications . . . 138
7.4.2.1 Resolution . . . 139
7.4.2.2 Dynamic range . . . 139
7.4.2.3 Linearity . . . 139
7.4.3 Standard Readout - time measurements specifications . . . 139
7.4.3.1 Resolution . . . 139
7.4.3.2 Dynamic Range . . . 140
7.4.3.3 Linearity . . . 140
7.4.4 Standard Readout - DCH Front End Electronics (overall design) . . . 140
7.4.5 Standard Readout - On Detector Electronics . . . 140
7.4.5.1 Preamplifier Boards . . . 140
7.4.6 Sampled Waveforms - specifications . . . 141
7.4.6.1 Resolution . . . 141
7.4.6.2 Dynamic range . . . 141
7.4.6.3 Linearity . . . 141
7.4.7 Sampled Waveforms - DCH Front End Electronics (overall design) . . . 141
7.4.8 Sampled Waveforms - On Detector Electronics . . . 142
7.4.8.1 Preamplifier Boards . . . 142
7.5 High Voltage system - Robertson, Martin 1 page . . . 142
7.5.1 Main HV system and cable routing - Robertson 0.5 page . . . 142
7.5.2 Distribution boards - Martin 0.5 page . . . 142
7.5.3 HV distribution boards - Standard ReadOut . . . 142
7.6 Gas system . . . 142
7.7 Calibration and monitoring - Roney 3 pages . . . 144
7.7.0.1 Slow control systems . . . 144
7.7.0.2 Calibration . . . 144
7.7.0.3 Gas monitoring system . . . 144
7.7.0.4 On-line monitor . . . 144
7.8 Integration . . . 144
7.8.1 Overall geometry and mechanical support . . . 144
7.8.2 Installation and alignment . . . 144
7.8.3 Services . . . 144
7.9 Bibliography . . . 146

8 Particle Identification **141**
8.1 Summary of Physics Requirements and Detector Performance goals . . . 141
8.1.1 Physics requirements . . . 141
8.1.2 Detector concept . . . 141
8.1.3 Charged Particle Identification . . . 142

8.2 Particle Identification Overview . . . 142
8.2.1 Experience of *BABAR* DIRC . . . 143
8.2.2 Barrel PID: Focusing DIRC (FDIRC) . . . 143
8.3 Projected Performance of FDIRC 2-3 pages . . . 147
8.3.1 Reconstruction Arnaud, Roberts . . . 147
8.3.2 MC Simulation . . . 147
8.3.3 Effect of Background on performance Roberts . . . 147
8.4 The Barrel FDIRC Detector Overview . . . 147
8.4.1 Photodetectors . . . 147
8.4.2 Laser calibration system . . . 157
8.4.3 FDIRC Mechanical Design . . . 159
8.4.4 Electronics readout, High and Low voltage . . . 169
8.4.5 Integration issues . . . 174
8.4.6 FDIRC R&D Results until now . . . 175
8.4.7 Ongoing FDIRC R&D . . . 178
8.4.8 System Responsibilities and Management . . . 178
8.4.9 Cost, Schedule and Funding Profile . . . 178
8.5 A possible PID detector on the Super*B* forward side . . . 180
8.5.1 Physics motivation and detector requirements . . . 180
8.5.2 Forward PID R&D activities . . . 181
8.5.3 The Forward task force . . . 184
8.5.4 The DIRC-like forward time-of-flight detector (FTOF) . . . 186

9 Electromagnetic Calorimeter 197
9.1 Overview . . . 197
9.1.1 Background and radiation issues . . . 198
9.1.2 Simulation tools . . . 199
9.1.2.1 Fastsim . . . 199
9.1.2.2 FullSim . . . 199
9.2 Barrel Calorimeter . . . 200
9.2.1 Requirements Relevant to the Super*B* Environment . . . 200
9.2.1.1 Crystal Aging at *BABAR* . . . 200
9.2.1.2 Backgrounds . . . 200
9.2.2 Description of *BABAR* Barrel Calorimeter . . . 201
9.2.2.1 Mechanical design . . . 201
9.2.2.2 Readout . . . 203
9.2.2.3 Low-energy Source Calibration . . . 205
9.2.2.4 Light Pulser . . . 207
9.2.3 Performance of *BABAR* barrel . . . 207
9.2.3.1 Energy and position resolution . . . 207
9.2.3.2 Gamma-gamma mass resolution . . . 207
9.2.3.3 Radiation Damage Effects on Resolution . . . 209
9.2.3.4 Expected Changes in Performance at Super*B* . . . 209
9.2.4 Electronics changes . . . 210
9.2.4.1 Requirements . . . 210
9.2.4.2 Electronic noise measurements . . . 210
9.2.4.3 Readout design . . . 212

9.2.5 SLAC De-installation, Transport and Local Storage . . . 212
9.2.6 Electronics refurbishment . . . 212
9.2.7 Re-installation at Tor Vergata . . . 213
9.3 Forward Calorimeter . . . 213
9.3.1 LYSO Crystals . . . 214
9.3.1.1 Introduction . . . 214
9.3.1.2 Optical and Scintillation Properties . . . 214
9.3.1.3 Radiation Hardness . . . 219
9.3.1.4 Specifications, Production and Testing . . . 221
9.3.2 Readout and Electronics . . . 221
9.3.2.1 APD Readout . . . 221
9.3.2.2 Electronics Design . . . 223
9.3.2.3 Requirements on mechanics . . . 223
9.3.3 Calibrations . . . 223
9.3.3.1 Initial LYSO calibration with source . . . 223
9.3.3.2 Electronics calibration . . . 224
9.3.3.3 Temperature monitoring and correction . . . 224
9.3.4 Mechanical Structure . . . 224
9.3.4.1 Crystals . . . 224
9.3.4.2 Modules . . . 226
9.3.4.3 Installation . . . 226
9.3.4.4 Refurbishment of the BaBar structure . . . 226
9.3.4.5 Spare FWD modules survey and tests . . . 227
9.3.5 Tests on Beam . . . 227
9.3.5.1 Description of apparatus . . . 227
9.3.5.2 Description of the beams . . . 228
9.3.5.3 Description of data and calibration . . . 229
9.3.5.4 Electronics noise measurements . . . 230
9.3.5.5 Temperature corrections . . . 231
9.3.5.6 Results . . . 231
9.3.6 Alternatives . . . 232
9.3.6.1 Full LYSO calorimeter . . . 232
9.3.6.2 Pure CsI . . . 235
9.3.6.3 BGO . . . 235
9.3.6.4 Comparison among options . . . 238
9.4 Backward Calorimeter . . . 238
9.4.1 Requirements . . . 240
9.4.1.1 Energy and angular resolution . . . 240
9.4.1.2 Background rates . . . 241
9.4.1.3 Radiation hardness . . . 242
9.4.1.4 Solid angle, transition to barrel . . . 242
9.4.2 Mechanical design . . . 243
9.4.2.1 Calorimeter construction . . . 244
9.4.2.2 Support and services . . . 244
9.4.3 SiPM/MPPC readout . . . 244
9.4.4 Electronics . . . 245
9.4.5 Calibration . . . 245

9.4.6 Backward simulation . . . 246
9.4.7 Performance in simulations . . . 246
9.4.8 Impact on physics results . . . 246
9.4.9 Use for particle identification . . . 248
9.4.10 Discussion of task force conclusions . . . 251
9.5 Trigger . . . 252
9.5.1 Calorimeter readout trigger . . . 252
9.5.1.1 Normal mode . . . 252
9.5.1.2 Calibration mode . . . 252
9.5.2 Calorimeter trigger primitives . . . 252
9.6 Environmental monitoring . . . 252

10 Instrumented Flux Return 259
10.1 Physics Requirements and Performance Goals . . . 259
10.2 Detector Overview . . . 259
10.2.1 The Absorber Structure . . . 259
10.2.2 The Active Detector Choice . . . 261
10.3 Backgrounds . . . 261
10.3.1 Main background sources . . . 261
10.3.1.1 Neutron Background . . . 261
10.3.1.2 Charged Particles . . . 262
10.3.1.3 Photon background . . . 263
10.3.2 Background remediation . . . 263
10.3.3 Radiation doses on the IFR detector . . . 264
10.4 Identification Performances . . . 264
10.4.1 Muon Detection . . . 264
10.4.2 K_L Detection . . . 266
10.5 Detector R&D . . . 266
10.5.1 Module Tests and Results . . . 267
10.5.1.1 Scintillators . . . 267
10.5.1.2 Fibers . . . 267
10.5.1.3 Photodetectors . . . 268
10.5.1.4 Other related studies . . . 269
10.5.1.5 New R&D studies... . . . 269
10.5.1.6 Radiation Damage Studies . . . 269
10.5.1.7 New Radiation Damage Studies . . . 269
10.5.2 Prototype Test and Results . . . 270
10.5.3 Design and construction of the IFR prototype . . . 270
10.5.3.1 Beam Tests . . . 271
10.5.3.2 Tests Results . . . 271
10.6 Baseline Detector Design . . . 273
10.6.1 System Layout . . . 273
10.6.2 Chamber Construction and Assembly . . . 274
10.7 Front-End Electronics . . . 274
10.7.1 Introduction . . . 274
10.7.2 Photodetectors and PCBs . . . 274
10.7.2.1 Photodetector PCB and optical coupling to fibers . . . 274

10.7.2.2 Optical coupling to fibers . . . 275
10.7.2.3 Photodetector location . . . 275
10.7.2.4 Photodetector choice . . . 276
10.7.2.5 Aging and background issues . . . 277
10.7.2.6 Temperature requirements . . . 277
10.7.3 IFR readout electronics: an overview . . . 278
10.7.3.1 Introduction . . . 278
10.7.3.2 Basic features of the IFR detector . . . 278
10.7.3.3 IFR channel count estimation . . . 279
10.7.3.4 Estimations of the IFR event size and data bandwidth . . . 279
10.7.3.5 Background radiation and electronics design constraints . . . 280
10.7.3.6 The IFR readout system . . . 283
10.8 Final assembly and installation . . . 291
10.9 ES&H issues . . . 292
10.10 Structure of the IFR group . . . 292
10.11 Cost and schedule . . . 292

11 Magnet and Flux Return **297**

12 Electronics, Trigger, Data Acquisition and Online **299**
12.1 Architecture Overview . . . 299
12.1.1 Trigger Strategy . . . 299
12.1.2 Trigger Rate and Event Size Estimation . . . 300
12.1.3 Dead Time and Buffer Queue Depth Considerations . . . 301
12.2 Trigger and Event Data Chain . . . 302
12.2.1 Choice of Global Clock Frequency . . . 302
12.2.2 Level-1 Trigger . . . 303
12.2.3 Fast Control and Timing System . . . 307
12.2.4 Control and Data Links . . . 310
12.2.5 Common Front-End Electronics . . . 314
12.2.6 Read-Out Modules . . . 315
12.2.7 Network Event Builder . . . 316
12.2.8 High-Level Trigger Farm . . . 317
12.2.9 Data Logging . . . 318
12.3 System Integration and Error Handling . . . 318
12.4 Control Systems . . . 318
12.4.1 Electronics Control System . . . 319
12.4.2 Detector Control System . . . 320
12.4.3 Farm Control System . . . 320
12.5 Other Systems . . . 320
12.5.1 Data Quality Monitoring System . . . 321
12.5.2 Other Components . . . 321
12.5.3 Software Infrastructure . . . 321
12.6 R&D for Electronics, Trigger and Data Acquisition and Online . . . 321
12.7 Conclusions . . . 322

13 Subdetector Electronics and Infrastructure **325**
13.1 Subsystem-specific Electronics . . . 325
13.1.1 SVT Electronics . . . 325
13.1.1.1 SVT Summary . . . 327
13.1.2 DCH Electronics . . . 327
13.1.2.1 Design Goals . . . 327
13.1.2.2 DCH Front-end system (block diagram) . . . 327
13.1.2.3 Standard Readout - OFF DETECTOR electronics . . . 328
13.1.2.4 Sampled Waveforms - OFF DETECTOR electronics . . . 329
13.1.2.5 Front End Crates . . . 330
13.1.2.6 Number of crates and links . . . 330
13.1.2.7 ECS . . . 330
13.1.2.8 Cabling . . . 330
13.1.2.9 Power Requirements . . . 330
13.1.2.10 DCH Summary . . . 331
13.1.3 PID Electronics . . . 331
13.1.3.1 The Front-end Crate . . . 331
13.1.3.2 The Communication Backplane . . . 332
13.1.3.3 The PMT Backplane . . . 332
13.1.3.4 Cooling and Power Supply . . . 332
13.1.3.5 The Front-end Board . . . 332
13.1.3.6 The Crate Controller Board (FBC) . . . 332
13.1.3.7 PID Summary . . . 333
13.1.4 EMC Electronics . . . 333
13.1.4.1 EMC Summary . . . 334
13.1.5 IFR Electronics . . . 335
13.1.5.1 IFR Summary . . . 338
13.2 Electronics Infrastructure . . . 338
13.2.1 Power supplies, grounding and cabling . . . 338
13.2.1.1 Power Supply to the Front-end: . . . 338
13.2.1.2 High Voltage Power Supply to the Detectors: . . . 342
13.2.2 Grounding and Shielding . . . 342
13.2.3 Cable Plant . . . 342

14 Software and Computing **345**
14.1 Tools to support detector studies . . . 345
14.1.1 Full Simulation . . . 345
14.1.1.1 Bruno: the SuperB full simulation software . . . 346
14.1.1.2 Geometry description . . . 346
14.1.1.3 Simulation input: Event generators . . . 346
14.1.1.4 Simulation output: Hits and MonteCarlo Truth . . . 347
14.1.1.5 Simulation optimization . . . 347
14.1.1.6 Staged simulation . . . 347
14.1.1.7 Interplay with fast simulation . . . 348
14.1.1.8 Long term evolution of the full simulation software . . . 348
14.1.2 Fast Simulation . . . 349
14.1.2.1 Event generation . . . 349

14.1.2.2 Detector description . . . 349
14.1.2.3 Interaction of particles with matter . . . 350
14.1.2.4 Detector response . . . 350
14.1.2.5 Reconstruction . . . 351
14.1.2.6 Machine backgrounds . . . 352
14.1.2.7 Analysis tools . . . 352
14.1.2.8 Simulation validation and detector studies . . . 353
14.1.3 Distributed computing tools . . . 353
14.1.3.1 Distributed resources . . . 354
14.1.3.2 Distributed systems design: a bird's-eye view . . . 355
14.1.3.3 The production system . . . 355
14.1.3.4 The data analysis system prototype . . . 357
14.1.3.5 The bookkeepieng and data placement database . . . 358
14.1.4 Collaborative tools . . . 359
14.1.4.1 Overview . . . 359
14.1.4.2 Authorization . . . 359
14.1.4.3 Portal System . . . 359
14.1.4.4 Document repository . . . 359
14.1.4.5 Documentation . . . 360
14.1.4.6 Code repository . . . 360
14.1.4.7 Code packaging and distribution . . . 361
14.2 Computing model outline . . . 361
14.2.1 Data processing . . . 362
14.2.2 Resource estimate . . . 362
14.2.3 Computing Infrastructure . . . 363
14.3 R & D program . . . 364
14.3.1 R& D on parallelization . . . 364
14.3.2 GPU R& D . . . 365
14.3.3 Framework R & D . . . 365
14.3.4 DIRAC framework evaluation . . . 368
14.3.4.1 Pilot jobs model . . . 368
14.3.4.2 Dirac data management . . . 369
14.3.4.3 DIRAC API . . . 369
14.3.4.4 User Management . . . 370
14.3.4.5 Tested Use Cases . . . 370
14.3.4.6 SuperBDIRAC module . . . 370
14.3.4.7 Building up a DIRAC Infrastructure for SuperB . . . 370
14.3.4.8 Future Works . . . 370
14.3.5 Data management and distributed storage R&D . . . 371
14.3.5.1 WAN data access . . . 371
14.3.5.2 Data access library . . . 372
14.3.5.3 File Transfer Service evolution . . . 372
14.3.5.4 Dynamic file catalogue technology . . . 372
14.3.5.5 Storage system evaluation . . . 372
14.4 Outlook . . . 373

15 Environmental Safety and Health **377**

16 Facilities, Mechanical Integration and Assembly **379**
16.1 Introduction 379
16.1.1 Magnet and Instrumented Flux Return 379
16.2 Component Extraction 380
16.3 Component Transport 381
16.4 Detector Assembly 382

17 The Super*B* Collaboration and Project Management **383**
17.1 Collaboration Membership 383
17.2 The Super*B* Collaboration Council 384
17.3 The Super*B* Spokesperson 385
17.4 The Super*B* Executive Board 385
17.5 The Super*B* Management Team and Management Plan 386
17.6 International Finance Review Committee 386
17.7 Interaction with the Cabibbo-Lab 386
17.8 Communications 386
17.9 Construction Responsibilities 387

18 Cost and Schedule **391**
18.1 Detector Costs 392
18.2 Basis of Estimate 396
18.3 Schedule 397

7 Drift Chamber

7.1 Overview - Finocchiaro, Roney 10 pages

7.1.1 Physics Requirements - 3 pages

7.1.2 Geometrical Constraints

The Drift Chamber inner radius is constrained by the final focus cooling system and by the Tungsten shield surrounding it to $R^{DCH}_{inner} = 265\,mm$, the outer radius is constrained to $R^{DCH}_{outer} = 809\,mm$ by the DIRC quartz bars. The total length available for the Drift Chamber is of $L^{DCH} = 2700$ mm. As the rest of the detector, the drift chamber is shifted by the nominal BABAR offset (367 mm) with respect to the interaction point.

Simulation studies performed on several signal samples with both high (*e.g.* $B \to \pi^+\pi^-$), and medium-low (*e.g.* $B \to D^* K$) momentum tracks indicate that:

a) as expected, momentum resolution improves

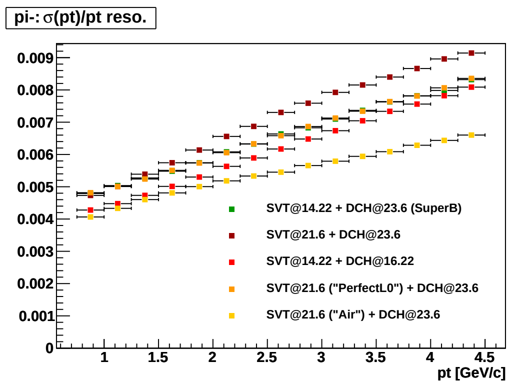

Figure 7.1: Track momentum resolution for different values of the drift chamber inner radius.

as the minimum drift chamber radius R_{min} decreases, see Fig. 7.1; R_{min} is actually limited by mechanical integration constraints with the cryostats and the radiation shields.

b) The momentum and especially the dE/dx resolution for tracks going in the forward or backward directions are clearly affected by the change in number of measuring samples when the chamber length is varied by 10−30 cm. However the fraction of such tracks is so small that the overall effect is also not large (*to be better quantified with updated FastSim studies*).

7.1.3 Machine Background Considerations - Cenci 3 pages

7.1.4 DCH Design Overview - 2 pages

7.1.5 Expected Performance - 2 pages

7.2 Design Optimization - Finocchiaro, Hearty, Piccolo, Roney 9 pages

The *BABAR* drift chamber operational record has been quite good, both for what performances and reliability is concerned; however there are possible paths of improvements that we have explored to try and design a drift chamber with performances yet better that the *BABAR* one.

7.2.1 Cluster Counting

A possibility being considered to improve the performances of the gas tracker is the use of the *cluster counting* method. Signals in drift chambers are usually split to an analog chain which integrates the charge, and to a digital chain recording the arrival time of the first electron, discriminated with a given threshold. The *cluster counting* technique consists instead in digitizing the full waveform to count and measure the time of all individual peaks. On the assumption that these peaks can be associated to the primary ionization acts along the track, the energy loss and to some extent the spatial coordinate measurements can be substantially improved. In counting the individual cluster, one indeed removes the sensitivity of the specific energy loss measurement to fluctuations in the amplification gain and in the number of electrons produced in each cluster, fluctuations which significantly limit the intrinsic resolution of conventional $\mathrm{d}E/\mathrm{d}x$ measurements.

The ability to count the individual ionization clusters and measure their drift times strongly depends on the average time separation between them, which is, in general, relatively large in He-based gas mixtures thanks to their low primary yield and slow drift velocity. Other requirements for efficient cluster conting include good signal-to noise ratio but no or limited gas-gain saturation, high preamplifier bandwidth, and digitization of the signal with a sampling speed of the order of 1Gs/sec. Finally, it is necessary to extract online the relevant signal features (*i.e.*the cluster times), because the DAQ system of the experiment would hardly be able to manage the enormous amount of data from the digitized waveforms of the about 10 000 drift chamber channels.

7.2.2 Cell Design and Layer Arrangement

The drift chamber cell design must optimise the homogeneity of the electric field inside the cell; this is particularly relevant with the non-saturated mixture we intend to use. Another critical parameter is the overall wire material, and an optimal use of the drift chamber volume for accommodating as many measurament points as possible.

The design for the Super*B* drift chamber employs small rectangular cells arranged in concentric layers about the axis of the chamber. The z coordinate of the track hits is measured by orienting a subset of the wire layers at a small positive or negative stereo angle, ε, relative to the chamber axis. Such a measurement is performed with precision $\sigma_z \simeq \sigma_{R\phi}/\tan\varepsilon$. As in *BABAR*, four consecutive cell layers are grouped radially into a superlayer (SL). This will allow to keep the same *BABAR* algorithms for track-segment finding, both in the track reconstruction and in the formation of the drift chamber trigger.

The rectangular cell layout ensures the most efficient filling of the drift chamber volume, because the transition between superlayers of opposite stereo angles does not require to leave free radial space, nor layers of field-shaping guard wires. Indeed, the latter are only used at a radius inside the innermost SL and at a radius outside the outermost SL. Such guard wires also serve the purpose to electrostatically contain very low momentum electrons produced from background particles showering in the DCH inner cylinder and in the SVT, or background-related backsplash from detector material just beyond the outer SL.

Simulations[1] have shown that a field:sense wire ratio of 3:1 ensures good homogeneity of the electric field inside the cells. In this configuration each sense wire is surrounded by 8 field wires.

The radial positions of the stereo wires in the j-th layer vary with the z coordinate, being larger at the endplates than at the center of the chamber by the "stereo drop" $\delta_j \equiv R_j^{\rm EP} - R_j$. The cell shapes are most uniform when $\delta_j = \delta$ is a constant for all layers: this is obtained by changing the stereo angle with the radius, by the relation $\tan\varepsilon_j = 2\delta/L_j\sqrt{2R_j^{\rm EP}/\delta - 1}$ (L_j is the chamber length at layer j).

Additional constraints used to determine the cell layout include:

a) the number of cells of width w_j on the j-th sense wire layer, $N_j = 2\pi R_j/w_j$, must be an integer number;

b) to keep a fixed periodicity in signal and high voltage distribution, it is convenient that the number of cells per layer is incremented of a fixed quantity ΔN when passing from a SL to the next one.

c) since the density of both physical tracks and background hits is higher at smaller radii, we choose to have smaller cells in the innermost layers of the drift chamber.

A possible choice for the drift chamber layout, obtained for $k = 4$, $\delta = 8\,\rm mm$ $\Delta N = 16$ is shown in Table 7.1. In this arrangement the two innermost SL's contain 1472 cells with height $h = 10\,\rm mm$ and widths $w = (10.2 \div 11.7)\,\rm mm$. The cells in the remaining superlayers have $h = 13\,\rm mm$ and $w = (16.1 \div 19.1)\,\rm mm$. There are a total of 7872 cells in the drift chamber. The first two superlayers have an axial orientation; this minimizes the occupancy from background hits due to low-momentum spiraling electrons which traverse the drift chamber along its axis (see Sec.7.1.3). The two external super layers are also axial. The fact that the innermost and outermost super layers do not exhibit the stereo drop deformation δ matches the axial simmetry of the inner and outer drift chamber cylinders. The six internal SL's have a stereo arrangement, with angles as shown in the Table.

Table 7.1: A possible drift chamber SL structure, specifying the number of cells per layer, the radius at the center of the chamber of the innermost sense wire layer in the SL, the cell widths, and wire stereo angles, which vary over the four layers in a SL as indicated.

SL	$N_{\rm cells}$	R [mm]	width [mm]	Angle [mrad]
1	176	286.0	10.2 – 11.3	0
2	192	326.0	10.7 – 11.7	0
3	144	369.0	16.1 – 17.8	+(63 – 66)
4	160	421.0	16.5 – 18.1	−(67 – 69)
5	176	473.0	16.9 – 18.3	+(70 – 72)
6	192	525.0	17.2 – 18.5	−(73 – 75)
7	208	577.0	17.4 – 18.6	+(76 – 77)
8	224	629.0	17.6 – 18.7	−(78 – 79)
9	240	689.0	18.0 – 19.1	0
10	256	741.0	18.2 – 19.1	0

The corresponding wire map in the region with angle $|\varphi| < 10°$ is shown in Fig. 7.2 at the center of the chamber (a) and at the endplates (b).

It is seen that the axial-stereo transition between SL 2 and SL 3 creates some additional radial space close to the endplates, which disappears at the DCH center. The opposite happens at the stereo-axial transition between SL 8 and SL 9. It is clear that the electric field should be as uniform as possible across layers to ease the drift chamber calibration; however, simulation studies have shown that the field distortion at the two transition radii is moderate and does not require to be compensated by layers of guard wires, which would add material and reduce the sensitive volume.

In Fig.7.3 we show the drift lines and the isochrone curves for two sample rectangular cells of the proposed Super$B$ drift chamber in a 90%He-10%iC$_4$H$_{10}$, in a 1.5 T magnetic field. The rectangular cells with field:sense wire ratio of 3:1 are indeed a satisfactory compromise, ensuring that the field lines are sufficiently contained within the cell and the isochrone lines are isotropic for most of the drift region, while at the same time the number of field wires is not excessively large.

7.2.3 Gas Mixture

The gas mixture for the Super*B* drift chamber is chosen to allow optimal resolution in the measurement of both momentum and energy loss. It must also be operationally stable (*e.g.*, have a wide high voltage plateau), and be little sensitive to photons with $E \leq 10\,\mathrm{keV}$ to help controlling the rate of background hits (see Sec. 7.1.3). Finally, aging in the chamber should be slow enough to match the projected lifetime of a typical High Energy Physics experiment (about 15 years). These requirements already concurred to the definition of the *BABAR* drift chamber gas mixture, (80%He-20%iC_4H_{10}). Indeed, a high Helium content reduces the gas density and thus the multiple scattering contribution to the momentum resolution. Good spatial resolution calls for high single electron efficiency and for small diffusion coefficient. The effective drift velocity in Helium-based gas mixtures is typically non saturated, therefore it depends on the local electric field, and on the Lorentz angle. This dependences can be taken into account by a proper calibration of the space-time relations and in principle do not pose limits to attaining the required spatial resolution. In practice, a careful choice of the cell shape (see the dicussion in Sec. 7.2.2), and a small value of the Lorentz angle are an advantage.

To match the more stringent requirements on occupancy rates of Super*B*, it could be useful to select a gas mixture with a larger drift velocity in order to reduce ion collection times and so the probability of hits overlapping from unrelated events. The *cluster counting* option would instead call for a gas with low drift velocity and primary ionization. As detailed in Section7.2.4, R&D work is ongoing to optimize the gas mixture.

7.2.4 R&D and Prototype Studies

In order to optimize the gas mixture for the Super*B* environment, and to asses both the feasibility and the operational improvements for the *cluster counting* technique a complete R&D

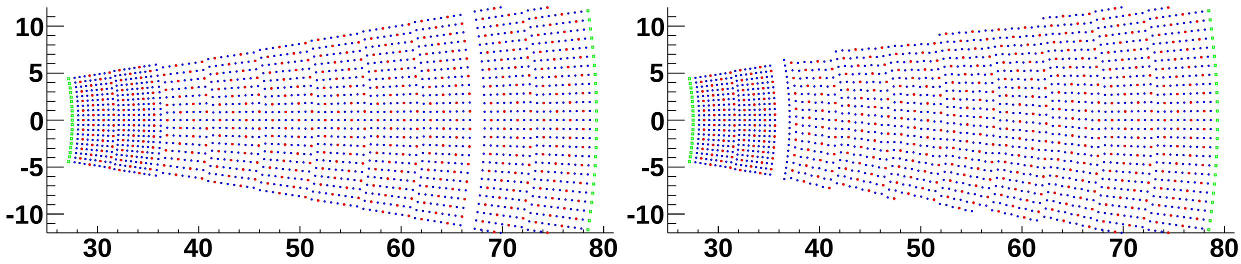

(a) Cell layout at the drift chamber center.

(b) Cell layout at the drift chamber endplates.

Figure 7.2: A possible cell layout of the Super$B$ drift chamber with $h_{\text{in}} = 10\,\text{mm}$, $h_{\text{out}} = 13\,\text{mm}$. Open green squares: guard wires; open blue circles: field wires; full red circles: sense wires. Note how the boundary regions after the first 8 layers of axially strung wires in the inner part of the chamber and after the following 24 layers of stereo layers map differently at the drift chamber center and at the endplates.

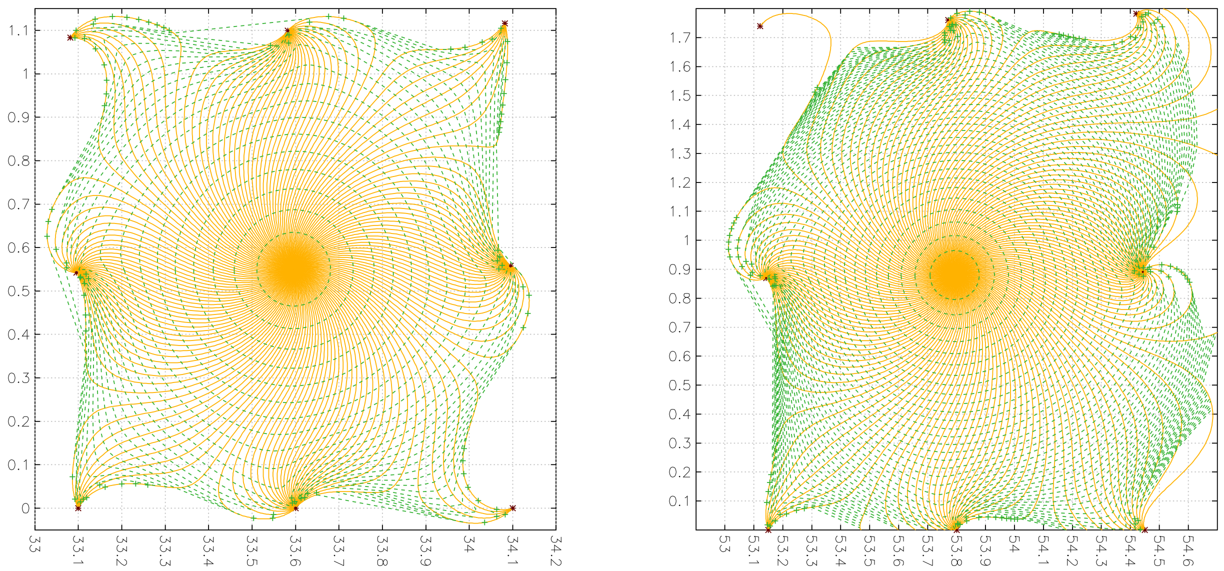

(a) Field and isochrone lines in a sample "smal" cell, on layer n. 6.

(b) Field and isochrone lines in a sample "big" cell, on layer n. 22.

Figure 7.3: Field lines and isochrone curves (shown with a 20 ns step) in a cell belonging to the first 8 layers (left) and in a larger cell of the outermost 32 layers (right).

Table 7.2: A possible drift chamber layer structure, specifying the number of cells per layer, the wire layer radius at the center of the chamber, the cell width and the wire stereo angle.

layer	N_{cells}	R [mm]	width [mm]	Angle [mrad]	layer	N_{cells}	R [mm]	width [mm]	Angle [mrad]
1	176	286.0	10.2	0.0	21	192	525.0	17.2	−72.9
2	176	296.0	10.6	0.0	22	192	538.0	17.6	−73.5
3	176	306.0	10.9	0.0	23	192	551.0	18.0	−74.2
4	176	316.0	11.3	0.0	24	192	564.0	18.5	−74.9
5	192	326.0	10.7	0.0	25	208	577.0	17.4	75.5
6	192	336.0	11.0	0.0	26	208	590.0	17.8	76.1
7	192	346.0	11.3	0.0	27	208	603.0	18.2	76.7
8	192	356.0	11.7	0.0	28	208	616.0	18.6	77.3
9	144	369.0	16.1	62.9	29	224	629.0	17.6	−77.8
10	144	382.0	16.7	63.9	30	224	642.0	18.0	−78.4
11	144	395.0	17.2	64.8	31	224	655.0	18.4	−78.9
12	144	408.0	17.8	65.7	32	224	668.0	18.7	−79.4
13	160	421.0	16.5	−66.6	33	240	689.0	18.0	0.0
14	160	434.0	17.0	−67.5	34	240	702.0	18.4	0.0
15	160	447.0	17.6	−68.3	35	240	715.0	18.7	0.0
16	160	460.0	18.1	−69.1	36	240	728.0	19.1	0.0
17	176	473.0	16.9	69.9	37	256	741.0	18.2	0.0
18	176	486.0	17.4	70.7	38	256	754.0	18.5	0.0
19	176	499.0	17.8	71.4	39	256	767.0	18.8	0.0
20	176	512.0	18.3	72.2	40	256	780.0	19.1	0.0

program has been proposed. The program includes both beam tests and cosmic ray stands to monitor performancs of *ad hoc* built prototypes. While the dE/dx resolution gain of the cluster counting method is in principle quite sizeable compared to the traditional total charge collection, the actual capability of the measured number of cluster might not retain the same analyzing power, due to a pletora of experimental effects that should be studied in detail so that the energy loss measurement derating should be assessed and, if possible, cured.

A few prototypes were built and operated to answer the above mentioned questions.

7.2.4.1 Prototype 1

The first one is a small aluminum chamber, 40 cm long, with a geometry resembling the the original *BABAR* drift chamber. It consists of 24 hexagonal cells organized in six layers with four cells each. A frame of guard wires with appropriate high voltage settings surrounds around the cell array to ensure uniformity of the electric field among the cells. The device was operated in a cosmic ray test stand in conjunction with an external telescope, used to extapolate the track trajectories with a precision of 80 μm or better . Different gas mixtures have been tried in the prototype: starting with the original *BABAR* mixture (80%He-20%iC_4H_{10}) used as a calibration point, both different quencher proportions and different quenchers have been tested in order to assess the viability of lighter and possibly faster operating gases.

As an example, the correlation between the extrapolated drift distance and the measured drift time is shown in Fig. 7.4 for a 75%He-25%C_2H_6 gas mixture. The result of a fit to a 5^{th}-order Chebychev polynomial is superimposed to the experimental points. Track-fit

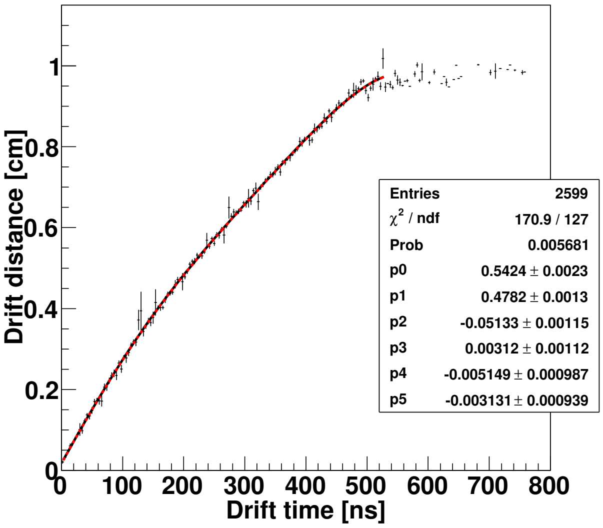

Figure 7.4: Track distance vs. drift time in a cell of the prototype. The line is the result of a fit with a 5^{th}-order Chebychev polynomial.

residuals and spatial resolution as a function of the drift distance for the same gas mixture are show in Fig. 7.5.

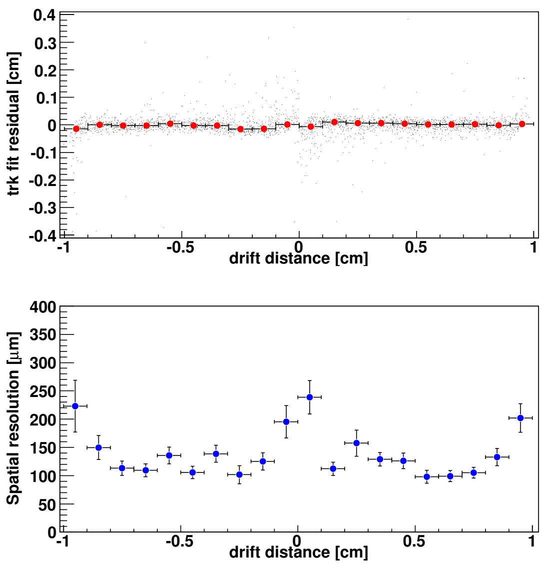

Figure 7.5: Track fit residuals (top) and spatial resolution (bottom) as a function of the drift distance.

7.2.4.2 Prototype 2

A full-length drift chamber prototype was designed, built and commissioned to study *cluster counting* in a realistic environment, including signal distortion and attenuation along 2.5 meter long wires. The prototype, which is also meant to serve as a test bench for the final Front-End electronics and for the drift chamber trigger, is composed by 28 square cells with 1.4 cm side, arranged in eight layers and – as in the final Super*B* drift chamber – with a field-to-sense wire ratio of 3:1. The eight layers have either 3 or 4 cells each, and are staggered by half a cell side to help reduce the left-right ambiguity. Tracks with angle $|\vartheta| \leq \pm 20°$ cross all the eight layers of the chamber. A set of guard wires surrounds the matrix of 28 cells to obtain a well-behaved field distribution at the boundary of the active detector volume. Most of the cells feature a 25 μm

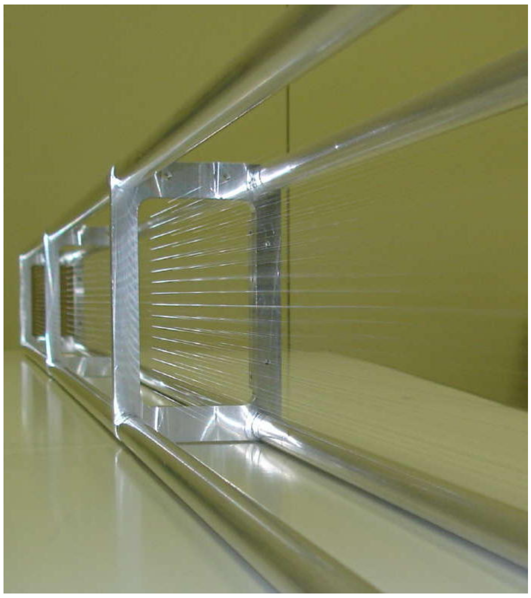

Figure 7.6: Prototype 2: detail of the strung wires.

Gold-plated Molybdenum sense wire, while for reference seven cells in two adjacent layers are strung with a 25 μm Gold-plated Tungsten wire, traditionally used in drift chambers. The reason for using the Molybdenum wire is its lower resistivity, therefore smaller dispersion for pulses travelling along the wires. A picture of the chamber after stringing completion is shown in Fig. 7.6. The entire wire structure is enclosed in

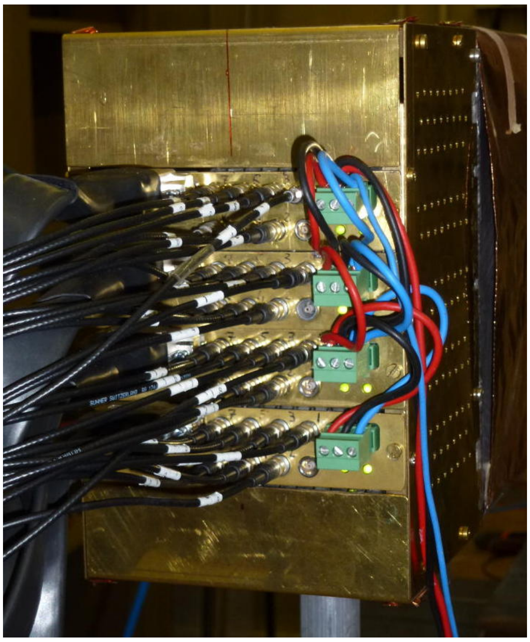

Figure 7.7: Prototype 2: FEE Faraday cage with signal and trigger cables.

an Aluminum container 3 mm thick; three pairs of thin windows have been carved in the middle and at the extremities in order to have smaller amount of material in the path of low energy particles measured by the device. Four preamplifier boards are used to extract the cell signals. Each board serves seven channels, each with a transimpedence preamplifier (rise time of about 2.4ns), at a nominal gain of 8mV/fC and a noise of 2200 e rms. Each boards also has a test input, both unipolar and differential outputs (50 Ω– 110 Ω); the latter are used for a test implementation of the Drift Chamber first level trigger. A detail of the Faraday cage housing the FEE boards and of the signal and trigger cables is shown in Fig. 7.7.

The data collected with this prototype are fed into a switch capacitor array digitizer[1], which samples the wire signals at 1 GS/sec with and input BW≥ 500 MHz. The challenge of detecting the ionization clusters in signals with a wide dynamic range and non-zero noise levels is apparent from the two sample waveforms shown in Figg. 7.8, recorded in the cosmic-ray setup. Hits associated to cosmic ray tracks reconstructed in the drift chamber prototype are used to compare the performances in the energy loss measurement of the traditional truncated mean algorithm and of the *cluster counting* method. Preliminary results when 10 samples from a single prototype cell are used to form a 70% truncated mean or to count the average number of clusters are shown in Fig. 7.9. In the experimental conditions of our test, *cluster counting* yields a 40-50% better relative resolution than the truncated mean method. Additional R&D efforts are ongoing to extend this encouraging result to different momentum regions, and study how the $K-\pi$ resolving power in the range of interest of Super$B$ ($|p| \leq 5$ GeV/c) improves with the *cluster counting* technique.

7.2.4.3 Single Cell Prototypes

Within the past year, the group has undertaken two beam tests of single-cell drift chamber prototypes at the TRIUMF M11 beam line. The goals of the tests were:

- to establish the benefits of clusters counting for particle identification;
- to study the suitability for cluster counting of various amplifier prototypes provided by the University of Montreal; and
- to quantify the impact on particle identification performance of various design choices, including sense wire diameter, cable for transmitting the analog signal, connectors, termination, and gas gain.

The beam test in November 2011 used a single prototype, with 25 μm diameter sense wire, while the test in summer 2012 used two prototypes, one with 20 μm sense wire, and the other with either 25 or 30 μm. The prototypes were 2.7m long, and consisted of a single 15 mm square cell surrounded by an array of

[1] CAEN V1742: http://www.caen.it/csite/CaenProfList.jsp?parent=13&Type=WOCateg

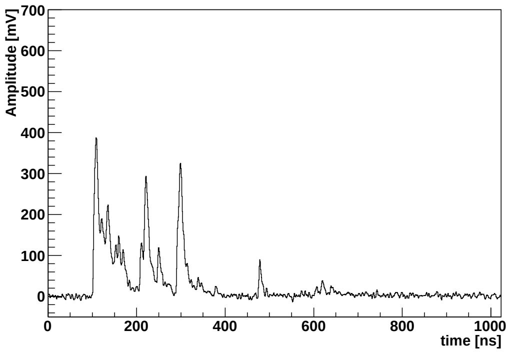

(a) Sample waveform n.1

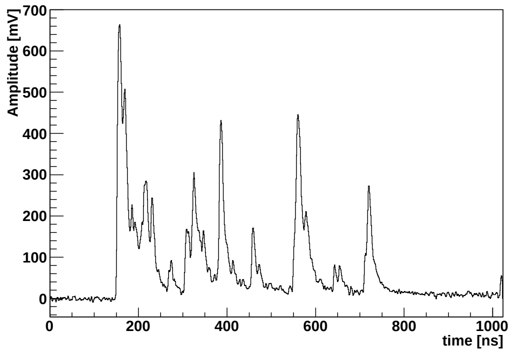

(b) Sample waveform n.2

Figure 7.8: Sample waveforms from two cells of the full-length drift chamber prototype.

bias wires that adjusted the electric field distribution within the cell to be that expected for a large drift chamber [Fig. 7.10]. A 90% helium / 10% isobutane (90:10) mixture was used for the summer 2012 tests, while the November 2011 test also tested 80:20 and 95:5.

J. P. Martin (U. Montreal) provided five different amplifier prototypes, with three different input impedances: 50, 170, and 380Ω. The impedance of the cell is 380Ω, and for most tests, the cell was terminated at this value on the non-readout end. The 170 and 380Ω consisted of an impedance-matching front end, followed by a 100$\times$ gain stage (of 50Ω input impedance); the 50Ω amplifier consisted only of this gain stage.

The TRIUMF M11 beam line was used for the tests [Fig. 7.11a]. Our tests used positively-charged electrons, muons, and pions, with momenta ranging from 140 to 350 MeV/c. In this momentum range, the particle identification separation between muons and pions is comparable to that between pions and kaons at the 2–3 GeV/c range relevant for Super$B$. The trigger and time-of-flight (TOF) system consisted of two scintillator counters, each with a pair of Burle micro-channel plate phototubes. The trigger rate was typically tens of Hertz, and the TOF resolution was 130 ps, providing clean separation between the particle species.

In the November 2011 test, the drift chamber waveforms were digitized using a CAEN switched-capacitor array, read out using the MIDAS data acquisition system. The bandwidth of this module is 300 MHz, which may be less than required for cluster counting, so in the Summer of 2012, a 4 GHz bandwidth LeCroy oscilloscope was instead used for digitization. In both cases, the amplifier and digitizer were connected by a

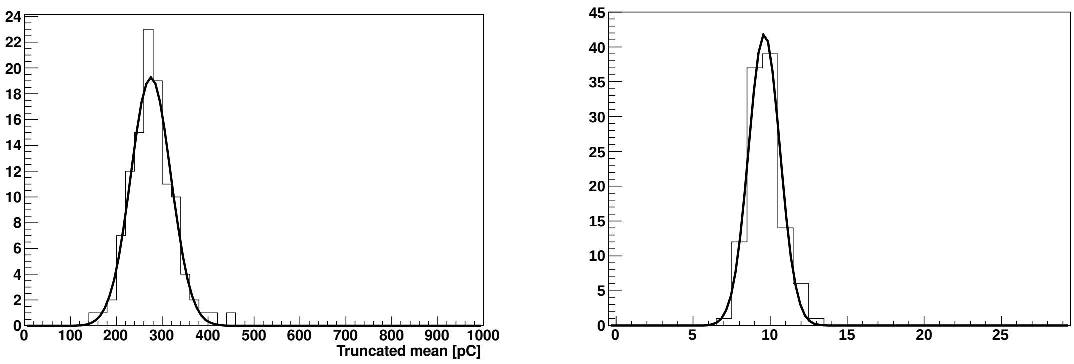

(a) Average dE/dx distribution

(b) Average n. of clusters

Figure 7.9: Average dE/dx and number of clusters from 10 samples of a single cell belonging to a track reconstructed in the prototype.

10 m long cable, the distance expected in the final design. Events were written to disk at 10–15 Hz. Figure 7.12 shows a typical waveform.

The benefits of cluster counting on particle ID performance are characterized by comparing the separation between muon and pion tracks using dE/dx only to the combination of dE/dx and cluster counting. Analysis is in progress, and results shown here are preliminary.

A track is formed by randomly selecting 40 samples of the same particle species as determined by the TOF system. The track dE/dx is obtained by discarding the largest 30% of the samples. Clusters are identified by a simple threshold on a smoothed version of the waveform. This algorithm is not necessarily optimal, and other methods are under study. Conversely, adequate performance may be achieved using a simpler algorithm that could be implemented in hardware, as opposed to an FPGA. The track is characterized by the average of the number of clusters in the 40 samples. The track dE/dx and cluster counting values are combined in a likelihood ratio that is used to label the track as a muon or pion. Figure 7.13 show examples of the results from the two beam tests. The addition of cluster counting significantly reduces the fraction of muons that are misidentified as pions.

7.2.4.4 Aging studies

The goal of the aging studies is to establish that the proposed drift chamber can survive for a lifetime of at least 100 ab^{-1}.

These studies use an ^{55}Fe source both to age a test chamber, and to characterize its

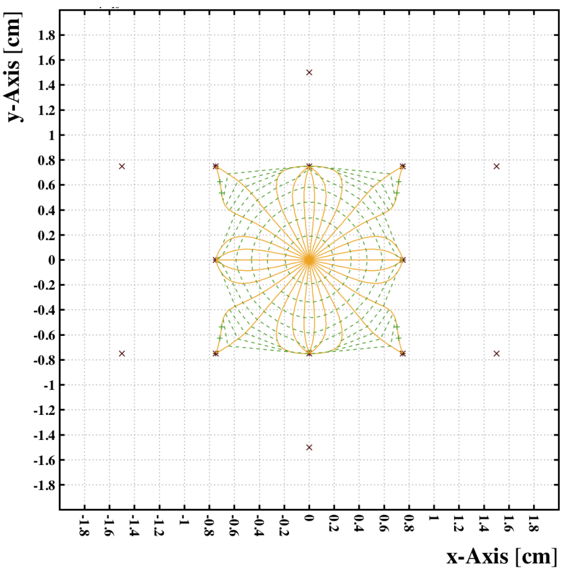

Figure 7.10: Cell design of the single cell prototypes.

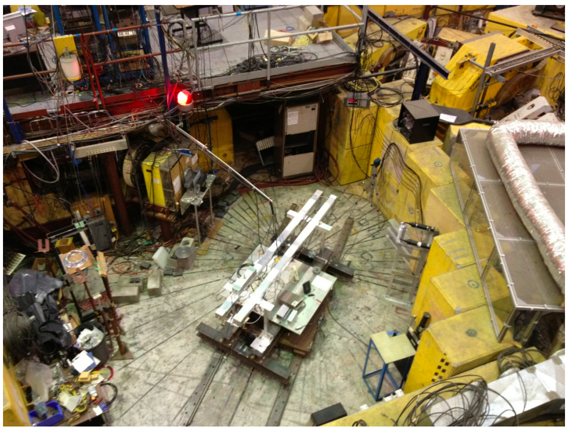

Figure 7.11: The M11 beam area at TRIUMF, showing two single-cell drift chamber prototypes under test in Summer 2012.

performance. The initial studies are using a 30 cm long chamber containing a single *BABAR*-like hexagonal-shaped cell, and an 80% helium 20% isobutane gas mixture. The sense wire is 20 micron gold-coated tungsten, and the field and bias wires are 120 micron gold-coated aluminum. The chamber is exposed to a 100 mCi ^{55}Fe source. The resulting current is monitored, along with temperature and atmospheric pressure, as a way to characterize gain as a function of accumulated charge. Once per week, the hot source is replaced with a low-intensity one and the pulse-height spectrum is recorded (Fig. 7.14). The location of the ^{55}Fe peak is an additional measurement of gain. The number of very small pulses is sensitive to the Malter effect, a form of aging of the field wires in which they accumulate an insulating coating. A second single-cell chamber, which is not exposed to the hot source, is used to calibrate out any possible gain effects due to gas variations, and to verify the gas density corrections. The chamber is operated at a voltage such that the electric field on the field wires is less than 20 kV/cm in order to minimize the Malter effect.

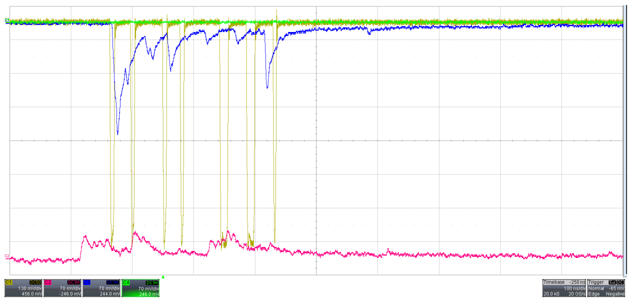

Figure 7.12: Waveforms recorded in Summer 2012 from a prototype with 20 μm sense wire (red) and 30 μm sense wire (blue), using two different 370Ω input impedance amplifier prototypes. The yellow curve shows the NIM logic signals from the time-of-flight system.

The aging chamber shows a gain drop of 25% after accumulating 310 mC/cm over the last 20 months. This lifetime is significantly in excess of the 34 mC/cm accumulated by the *BABAR* drift chamber. The *BABAR* chamber saw a 10% loss of gain over that time.

The next aging chamber is currently under construction. It will include seven square cells, so that the central field wires are surrounded by sense wires, and will therefore accumulate the correct amount of charge (Fig. 7.15). It will use Super*B* materials, gold-coated 20 micron Molybdenum sense wires, and 80 or 90 micron bare aluminum field wires, and 90:10 helium-

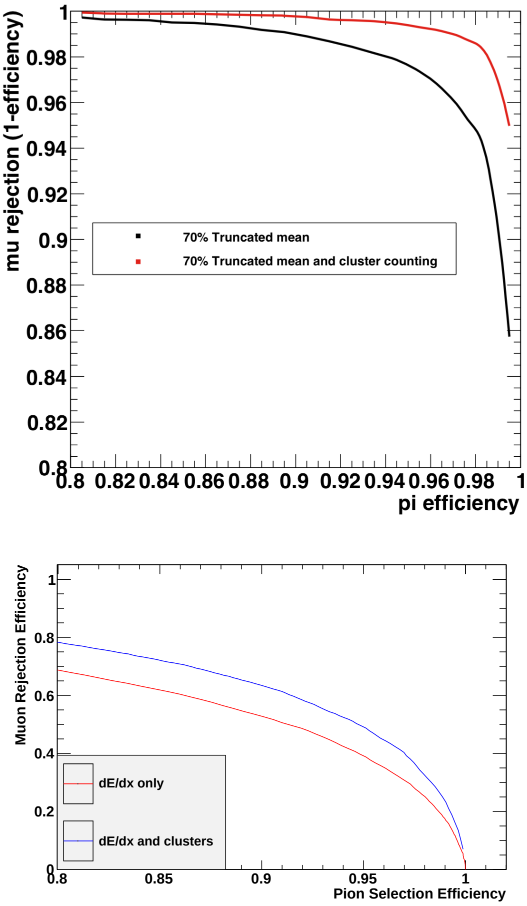

Figure 7.13: Fraction of muons identified as pions versus the fraction of pions satisfying the selection criteria, for dE/dx only, and for the combination of dE/dx and cluster counting. (a) 140 MeV/c data, November 2011 test; (b) 210 MeV/c data, summer 2012 test.

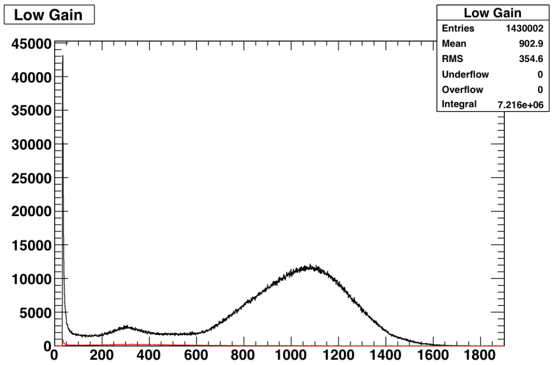

Figure 7.14: Pulse height spectrum recorded from an ^{55}Fe source by an aging chamber. The red curve is the underlying cosmic ray background.

isobutane gas. The structure of the chamber will be aluminum, as for the current aging chamber, but the walls will be covered by samples of the carbon-fiber material that will be used in the actual chamber.

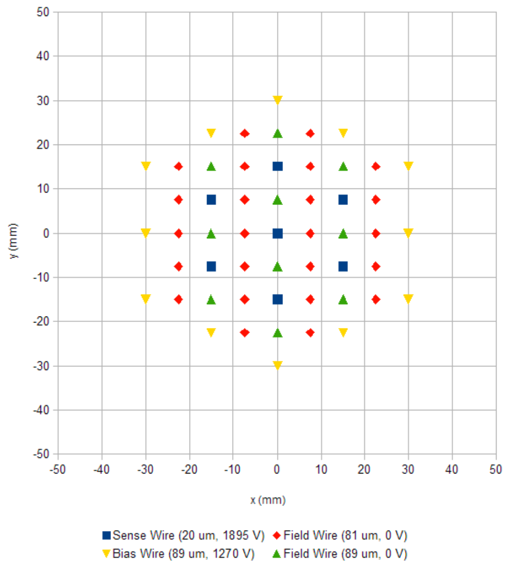

Figure 7.15: Wire layout of the new aging chamber under construction.

The amount of charge per cm expected for the Super$B$ chamber is a function of the chamber occupancy, the gas gain, and the total running time. Current background calculations indicate occupancy levels comparable to *BABAR*, including a five-times safety factor. The SuperB running time will also be comparable to BABAR. The gas gain may be higher, due to the requirements of cluster counting. The gas gain required is a function of the amplifier; the 50 ohm input impedance amplifier prototypes require four times the gas gain of the 370 ohm amplifiers, due to the impedance mismatch between the amplifier and the drift cell. The field wire diameter is, in turn, a function of the sense wire operating voltage, given the need to keep the electric field at the surface of the field wire below 20 kV/cm.

7.2.5 R&D Future Developments

- test beam with different particle species
- on-board feature extraction
- AOB

7.3 Mechanical Design

The drift chamber mechanical structure must sustain the wire load with small deformations, while at the same time minimizing material for the surrounding detectors. The structure is also required to ensure tightness for the gas filling the drift volume. We opted for a structure entirely in Carbon Fiber (CF) composite, with an approximately cylindrical geometry. A side view of the chamber is shown in Fig. 7.16.

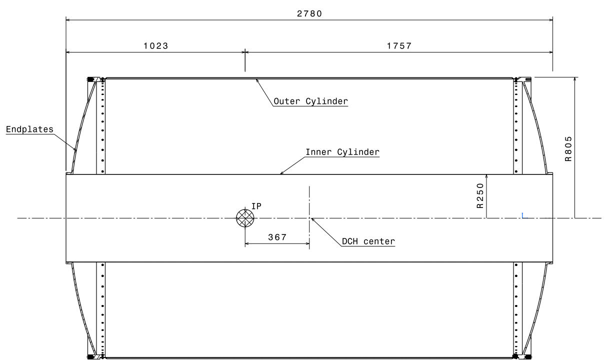

Figure 7.16: Longitudinal section of the DCH with principal dimensions.

7.3.1 Endplates

The wires defining the cell layout are strung between the two endplates, which are required to:

a) sustain the total wire load of XXXX tons (or N) (see sec. ??) with minimal deformations;

b) be as transparent as possible to avoid degrading the performances of the forward calorimeter.

c) have XXXXX precisely machined holes to allow positioning the crimp feed-throughs with tolerances better than XXXX μm;

The endplates are two identical pieces of 8 mm thick CF composite with inner radius of 250 mm and outer radius of 805 mm. Deformations under load can be minimized using for the endplates a shaped profile. An optimization taking into account different constraints resulted in spherical convex endplate, with a radius of curvature of 2100 mm. Two CF stiffening rings on the inner and outer rims help preventing radial (axial) deformations. An intermediate modulus carbon fiber (as T300 (XXXX), with a Young modulus of XXXXX) will be used. It is expected that the average material characteristics will be degraded by about 30 % or less after drilling the XXXX holes on the endplates. Detailed studies on this aspect will be performed on custom samples. The maximum displacements on the endplates is calculated to be less than 300 μm (Figure ??).

7.3.2 Inner cylinder

The drift chamber inner cylinder should be as transparent as possible to minimize the multiple scattering degradation to the p_T measurement. For this reason it was designed as a non load-bearing structure: it must only guarantee gas tightness, and sustain possible differential pressures of the order o 10 mbar between the inside and outside of the chamber. It is a thin (200 μm) CF cylinder of 250 mm radius, with a 25 μm aluminum foil glued on it as RF shield. During the stringing phase the inner cylinder will be free to move longitudinally being fixed only to one

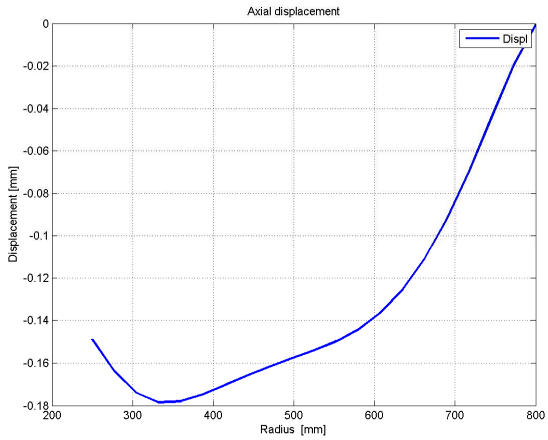

Figure 7.17: Displacement of each endplate due to the wire load.

endplate. Only after stringing, when all endplate deformations are settled, it will be glued to the other endplate.

7.3.3 Outer Cylinder

In addition to guaranteeing gas tightness and withstanding a differential pressure as the inner cylinder, the outer cylinder will also carry the wire load. It will be installed after completion of the wire stringing. To ease the construction and the mounting procedures, the cylinder is longitudinally divided in two half shells. Each shell consists of two 1 mm-thick CF skins laminated on a 6 mm-thick honeycomb core. Two thin aluminum foils, 100 μm on inside surface and 25 μm on outside surface, are glued to the shells to ensure the rf shield. The sandwich structure guarantees a high bending stiffness and a high safety factor for global buckling.

7.3.4 Choice of wire and electrostatic stability

7.3.5 Feedthrough design

The feedthroughs locate the wires to within the specified tolerances, hold the wire tension, and, in the case of the sense wires, insulate against the high voltage. They must achieve these goals while maintaining a helium-tight gas seal.

A feedthrough is made from two components, a plastic outer insulator, and a conducting crimp pin (Fig. 7.18). The insulators are injection-molded parts formed from Celenex 3300-2, chosen for its low shrinkage during molding, dimensional stability, and high dielectric strength. The crimp pins for the aluminum field wires are aluminum 6063. Studies are planned to determine whether copper or aluminum crimp pins are more suitable for the molybdenum sense wires. The crimp pins will have a gold-flash coating with a nickel underlayment.

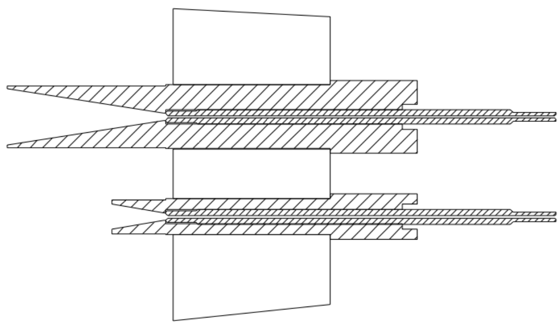

Figure 7.18: Sense wire (top) and field wire (bottom) feedthroughs from the *BABAR* drift chamber. The SuperB parts will be similar.

The two parts are glued together with an epoxy that is dyed so that extraneous epoxy on the crimp pin can be identified and removed.

The tolerances are specified to ensure that the contribution to cell resolution is small, with tolerances on the sense wire parts significantly tighter than those on the field wires. Inner diameter of sense wire crimp pins at the wire release point will be 100 microns, and 200 microns for field wires. Concentricity of the pin hole with respect to the shaft diameter will be less than 30 microns, and eccentricity of the shaft will be less than 25 microns.

Each of the approximately 75000 feedthroughs will be individually tested against the specifications. Sense wire feedthroughs will have an additional test to verify HV performance.

7.3.6 Endplate systems

7.3.6.1 Electronics enclosures

The amplifiers mounted on the backward endplate of the drift chamber, and the high-voltage components mounted on the forward endplate are covered by the electronics enclosures. The volumes are filled with nitrogen to ensure that a leak of the flammable drift gas through the endplate cannot form an explosive mixture. The enclosures also protect the components inside, and provide the mounting points for the chamber as a whole.

The enclosures are light aluminum structures (Fig. 7.19). The main features are feedthroughs for the various signals and services used by the chamber: chamber gas, nitrogen, cooling water, amplifier power and signal, and high voltage. Each $1/16^{\text{th}}$ sector corresponds to approximately 500 signal cables, arranged into 8-channel ribbon cables and feedthroughs. These feedthroughs may also carry the power and control lines for each amplifier. The feedthroughs are mounted on removable panels, while the cooling lines are on the fixed ribs. The panels allow access for installation and repairs, although such accesses are expected to be rare. Although the endplates are curved, the panels can be flat, reflecting the geometries of the backwards calorimeter and the forward time-of-flight system on either side of the drift chamber. This will greatly simplify the necessary gas seals.

7.3.6.2 Cooling

The fast amplifiers mounted on the drift chamber endplates produce approximately 1200 W of heat. This heat must be removed to keep the temperature of the drift chamber and nearby detectors stable and uniform. The cooling system to accomplish this will be water based, operating at a pressure below atmospheric pressure. Small leaks will therefore cause air to leak into the water, rather than leading to water leaking into the electronics enclosure. The system is quite similar to one recently built for the near detector of the T2K experiment.

The major components of the system include two water reservoirs, one at atmospheric pressure, and the other maintained at an absolute pressure of 0.3 atmospheres; a pump to move water between the systems; cooling lines to the drift chamber and inside the electronics enclosures; valves and gauges; a heat exchanger that connects to the laboratory chilled water system; and a control system to maintain the desired water temperature. Appropriate corrosion inhibitors and microbiocides will be added to the water. The lines within the enclosures will be mounted to the fixed ribs, and may include fins or other features to increase the surface area. These features, combined with turbulent nitrogen flow in the enclosure, may generate sufficient thermal flow from the amplifiers to keep the temperatures at an acceptable level. Mock-ups and thermal calculations will be undertaken to test this concept. The alternative will be cooling straps.

Although there is no heat generated on the forward endplate, cooling lines will be run to

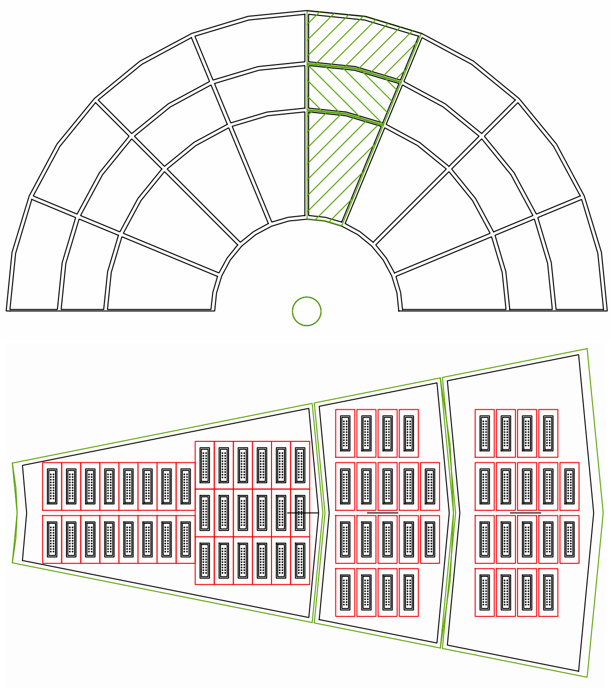

Figure 7.19: (a) The rib structure of each enclosure is machined from a solid piece of aluminum. (b) The feedthroughs are on panels mounted to the ribs.

ensure a uniform temperature across the drift chamber.

7.3.6.3 Shielding

The aluminum structure of the electronics enclosures, together with the aluminum skins on the outer and inner cylinders, form a Faraday cage that encloses the amplifiers and the chamber wires. A 25 micron thick aluminum skin bonded to the endplates provides additional shielding between the chamber wires and the enclosure volumes.

7.3.6.4 Electromechanical boards

Electrical connections to the crimp pins are required at both ends of every wire. At the forward end, the HV distribution boards ground the field wires and provide HV to the sense wires via the circuit described in Sec. 7.5, and terminate the sense wire at the characteristic impedance of the cell. At the backwards end, service boards ground the field wires, and gather the signals from eight sense wires onto a single multi-conductor connector. The only active components on the service boards are the HV blocking capacitors.

Each of the ten superlayers requires a different size of HV distribution board and service board. Only a single style of 8-channel preamp card is required. Each board will service eight cells (four in radius by two in azimuth), typically corresponding to 32 crimp pins. A number of crimp pin connections much larger than this would make the board difficult to insert and remove.

The connections to the crimp pins are made using low-insertion-force connectors, such as the Hypertronics connectors used for *BABAR*. The details of how the curvature of the endplate is handled in the design of the cards will require prototypes and mockups.

Jumpers between adjacent boards will connect the ground planes. At the HV end, jumpers will distribute the HV among the typically three boards serviced by a single HV channel.

The endplate will include two blind holes per board that will be used with dowel pins to align the boards during insertion. We do not anticipate using pull-down screws, which would require a large number of tapped holes in the endplates. Each board will have two threaded holes that will be used to push against the endplate if it is necessary to remove the board. The boards will be removed rarely, if ever. One of the two holes will be used during normal operations to provide an electrical connection to the aluminum RF shield on the endplate via a low-force spring connection.

7.3.7 Stringing

7.4 Electronics - Felici, Martin 1 page

7.4.1 Design Goals

The Super*B* Drift Chamber (DCH) front-end electronics is designed to extract and process approximately 8000 sense wire signals to:

- measure the electrons drift times to characterize a track (momentum of charged particles)
- measure the energy loss of particles per unit length, dE/dx (particle identification)
- provide hit information to the trigger system (trigger primitives)

Two scenarios will be investigated for the energy loss measurements. The first one is based on the measurement of the integrated charge on each sense wire, discarding the largest charge values to remove the Landau tails (Standard Readout), while the second one is based on the counting of the primary electron clusters (Sampled Waveforms). Because the front-end requirements for the two options are quite different, each option will be discussed in a separate section.

7.4.2 Standard Readout - charge measurements specifications

The method is based on integrated charge measurement thus allowing the use of (relatively)

low bandwidth preamplifiers. This makes the front-end chain less sensitive to noise pickup and instabilities, a suitable condition in a system with a large number of channels.
The three main specifications for a charge measurement are: resolution, dynamic range and linearity.

7.4.2.1 Resolution

Charge measurements for particle identification aim to measure the particle most probable energy loss, to a precision of the order of 7.5% despite the large fluctuations present in a single measurement.
The goal can be achieved by sampling many times the collected charge and applying the "truncated mean" method to resolve the distribution peak value to a precision of several percent.
Because the Super$B$ DCH design parameters and expected working conditions aim for an overall single cell resolution (σ_E) of about 35% and σ_E is mainly driven by the detector contribution, we can set a limit of 15% of the resolution for the front-end electronics contribution (i.e. $\sigma_{EL} \sim 5\%$) which can be neglected since $\sqrt{\sigma_E^2 + \sigma_{EL}^2} \sim \sigma_E$.
Finally, if we assume that the charge collection due to a minimum ionizing particle crossing orthogonally the cell is about 50 fC ($\sim 2fC/e$ @ 10^5 nominal gas gain) we can infer a limit to the Equivalent Noise Charge (ENC) for a single front-end channel of about 50 $fC \cdot 0.05 \simeq$ 2.5 fC.

7.4.2.2 Dynamic range

With 8 bits ADCs the dynamic is $2.5 - 500$ fC. This is more than necessary to satisfy the system requirements.

7.4.2.3 Linearity

As stated above, a single cell energy resolution is about 35%. Therfore a linearity of the order of 2% largely satisfies the system requirements.

7.4.3 Standard Readout - time measurements specifications

As for charge measurements, we have three main specifications: resolution, dynamic range and linearity.

7.4.3.1 Resolution

One of the Super$B$ DCH requirements is the charged particle tracks reconstruction. The measurement consist of recording the arrival time at the sense wire of the first ionized electron. This is done with a high precision compared to the spatial resolution (σ_S) of $\sim 110\mu m$. Contribution to σ_S are due to primary ionization statistics, electrons diffusion times and time measurement accuracy.
Assuming an intrinsic chamber resolution (σ_{SC}) of about 100 μm **(ref DCH)** the upper limit for the electronic contribution can be deduced to be $\sigma_{EL} \leq \sqrt{\sigma_S^2 - \sigma_{SC}^2} \simeq 50$ μm. As helium based gas mixtures are characterized by a non saturated drift velocity up to high fields, [5] this velocity rapidly increases as the electrons approach the sense wire. A value of 2.5 $cm/\mu s$ (25 $\mu m/ns$) [6] has been used to evaluate the maximum acceptable error in a time measurement, that is $\sigma_t \leq 50[\mu m]/25[\mu m/ns] \simeq 2$ ns.
Discarding the bunch length contribution (tenths of ps) there are two main error sources in time measurements: the discriminator jitter and the TDC resolution (digitization noise). The discriminator jitter, in turn, has two main contributions: signal noise and time-walk.
The signal noise contribution is generally small and can be evaluated according to $\Delta t = \sigma_{noise}/(dV/dt) \simeq \sigma_{noise} \cdot \tau/V_{max}$ where τ is the preamplifier-shaper peaking time. Assuming that a single electron cluster generates a signal of amplitude ~ 20 mV, and that the noise and the peaking time associated with the signal are $\sigma_{noise} \sim 3$ $mV(rms)$ and $\tau \sim 5$ ns we get a noise contribution to the time resolution of about 0.8 ns.
The time-walk effect is caused by the signal amplitude variation. With a peaking time of about 5 ns, a time-walk contribution for a low-threshold leading-edge discriminator can be es-

timated to be about 1.5 ns.
Finally, the digitization noise depends on the digitization unit Δ according to the formula $\sigma = \Delta/\sqrt{(12)}$. Using $\Delta \simeq 1.5$ ns a digitizing noise of about 0.45 ns is obtained.
In summary, without corrections, the time resolution is dominated by time-slewing effects thereby can be estimated to be about 1.8 ns (including all contributions). Nevertheless corrections can be applied using digitized signals to minimize time-slewing effects then reducing the time walk contribution (Fig. ??).

7.4.3.2 Dynamic Range

The TDC range depends on the drift velocity and on the cell size. A maximum drift time of about 600 ns has been estimated for Super$B$ DCH cells. Providing some safety factor, a TDC range of about 1 μs is enough to include any jitter in trigger generation and distribution.

7.4.3.3 Linearity

A linearity of the order of 1% fully satisfies time measurement requirements.

7.4.4 Standard Readout - DCH Front End Electronics (overall design)

The DCH FEE chain (Fig. ??) is split in two blocks: ON DETECTOR and OFF DETECTOR electronics.
In the following paragraphs we will give a description of the ON DETECTOR electronics while the description of the Off Detector Electronics can be found in Sec. 13.1.2.

7.4.5 Standard Readout - On Detector Electronics

7.4.5.1 Preamplifier Boards

Preamplifier boards will contain HV blocking capacitors, protection networks, preamplifiers and (eventually) shapers-amplifiers. Because of the small cell dimensions many cells can be grouped in a single, multi-channel preamplifier-shaper board. Signals and power supply cables will be connected to the boards by means of suitable connectors.
In addition to the requirements on the Signal to Noise Ratio (SNR), each preamplifier should be characterized by enough bandwidth to preserve signal time information and have low power requirement, not more than $20 \div 30$ mW per channel, to limit the total power dissipation on the backward end-plate to $160 \div 240$ W, thus allowing the use of simpler and safer forced air based cooling system (no risk of leak).
Concerning the circuit implementation, since the channel density is low and simple circuit can be used, an approach based on SMT technology can be adopted thus avoiding a specially designed (and expensive) ASIC development.
As an example, the simulation of a three stages transimpedance preamplifier based on SiGe transistors has been carried out. The first stage dominant pole is around 26 MHz while other stages have been designed with wider bandwidth thus resulting in a good separation in terms of cutoff frequencies.Simulation results

Table 7.3: Preamplifier main specifications

Linearity	$< 2\%(1-100fC)$
Output Signal Umbalance	$< 2\%(1-100fC)$
Gain (Differential)	~ 5.2 mV/fC
Z_{IN}	110 Ω
Z_{OUT}	50 Ω
Rise time	~ 2 ns ($C_D = 24pF$)
Fall time	~ 13 ns ($C_D = 24pF$)
Noise	1350 erms ($C_D = 24pF$)
V_{SUPPLY}	4V
P_D	$\sim$ 30mW

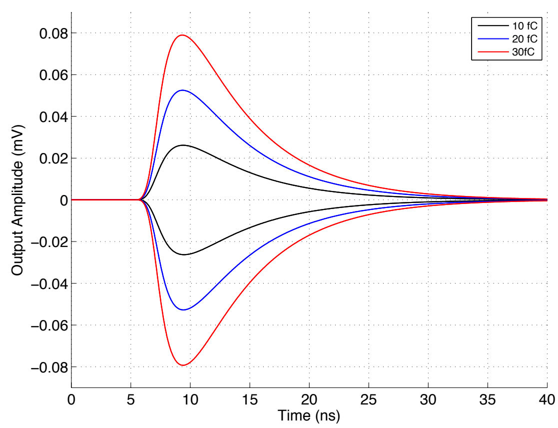

Figure 7.20: Preamplifier output for a 10, 20 and 30 fC test pulse ($C_{DET} = 24$ pF)

are given in table 7.3 while Fig. 7.20 shows the (simulated) output waveforms for 3 different input charges (10, 20 and 30 fC) injected through the test input.

7.4.6 Sampled Waveforms - specifications

Cluster Counting technique is very powerful as it leads to an improved particles identification. The method is based on the measurement of primary ionization. To fully exploit the technique, individual electrons clusters must be identified. In our system we use slow drift gas mixtures ($\sim$1 $\mu s/cm$), state of the art high sampling frequency digitizers (at least 1 GSPS) and fast processing (data throughput must sustain the Super$B$ expected 150 kHz average trigger rate). These modules require a large amount of power forcing us to limit the number of channels to 8/16 channels per Amplifier Digitizing Board (ADB). Also on the preamplifiers side fast amplifiers must be used resulting in a larger power requirements than for "Standard Readout". As a consequence, we are considering the use of a local liquid cooling system. The wide bandwidth requirement has also an impact on the type of cables used to interconnect preamplifiers and ADBs and on the full system noise pick-up sensitivity.
In addition the use of the Cluster Counting technique requires that the signal reflection in the sense wires be eliminated. This is done by means of termination resistors (R_T) that result in a lower limit on the system intrinsic noise.
Concerning the tracking requirements, if we assume 100% efficiency in the detection of each electron cluster, then the Cluster Counting dE/dx measurements includes information for tracking purposes This requires to store the arrival time of the clusters at the sense wires instead of simply counting them.
Specifications for the Sampled Waveforms measurements are the same we defined for the Standard Readout. That is: resolution, dynamic range and linearity.

7.4.6.1 Resolution

The resolution of of the digitizers depends on the lowest signal amplitude to be sampled and the system baseline noise. Assuming an average input signal of $\sim 6fC/e$ @ $3 \cdot 10^5$ gas gain, a preamplifier-shaper gain of $10mV/fC$ and a safety factor of 2 for gas gain fluctuations the average cluster signal is about 30 mV for a single electron.
We can estimate the preamplifier ENC from the contribution of the dominant noise source, that if of the termination resistor. Assuming a $CR - RC$ shaping circuit and a 3 ns peaking time we get an ENC of about 0.2 fC, that is about 2 mV rms for a preamplifier gain of 10 mV/fC.Thus a voltage resolution of about 2 mV allows a good control of system noise and cluster signals reconstruction.

7.4.6.2 Dynamic range

The Cluster Counting method requires the observation of peaks (corresponding to the clusters) in the digitized signals. The signal dynamic range (discarding gas fluctuations) is then given (as an upper limit) by the expected total ionization.Helium based gas mixture have already been well characterized [7]. We can assume that a m.i.p. crossing orthogonally a 1.2 cm square cell, filled with a 90/10 He/Iso gas mixture, will generate about 22 electrons. Thus an 8 bits ADC dynamic range is fully adequate for Cluster Counting measurements.

7.4.6.3 Linearity

As we are interested in finding (and tagging) signal peaks, a resolution of 2% fully satisfies the requirements.

7.4.7 Sampled Waveforms - DCH Front End Electronics (overall design)

The Sampled Waveforms DCH FEE chain is similar to the Standard Readout one. In this scenario we will have electronics modules connected by means of mini coaxial cables. Because of the smaller number of channels per ADB both the number of crates and ADBs will increases significantly (tables 13.4 and 13.6).

7.4.8 Sampled Waveforms - On Detector Electronics

7.4.8.1 Preamplifier Boards

Because preamplifier boards will host high bandwidth (∼ 350 MHz) amplifiers the layout and assembly are more difficult compared to the Standard Readout scenario. Particularly, special attention must be provided to avoid ground loops to minimize instabilities and external noise pickup.

.

.

Something about preamplifier ......

.

.

7.5 High Voltage system - Robertson, Martin 1 page

7.5.1 Main HV system and cable routing - Robertson 0.5 page

7.5.2 Distribution boards - Martin 0.5 page

7.5.3 HV distribution boards - Standard ReadOut

The high voltage distribution network will be located on the forward end-plate. The distribution board modularity will match the preamplifier modularity while the number of distribution boards connected to a single HV channel will depend on the layer (example: inner layers = 2 boards, outer layers = 5 boards).

The HV distribution system consists of power supplies and distribution boards, along with associated cables, feedthroughs into the forward electronics enclosure volume and HV distribution within that volume. The voltage will be supplied by a CAEN SY4527 Universal Multichannel System supply with 16 A1535N distribution boards, giving a total of 384 channels. This is sufficient granularity that a single channel failure will have a small impact on detector performance. Spares of both the SY4527 and the A1535N will be on hand. The A1535N permits individual channels to operate in current-generator mode in case of over-currents. This feature was found to be extremely useful for the *BABAR* drift chamber as it permitted the chamber to handle locally high background rates without ramping down the chamber HV.

Individual HV channels are brought to the drift chamber from the A1535N boards via multistrand cables terminating at both ends with A996 52 pin Radiall connectors.

The multiconductor cable connects to a filter box containing a low-pass filter, located at the inner radius of the forward enclosure. The individual channels are fanned out within the enclosure to the HV distribution boards (Sec. 7.3.6). Each HV channel supplies two or three 8-channel distribution boards, depending on the superlayer.

The HV distribution and sense wire termination circuitry is shown in Fig. 7.21. If termination is not used, the termination resistor (R_T) and the 500 pF capacitor per sense wire are not needed.

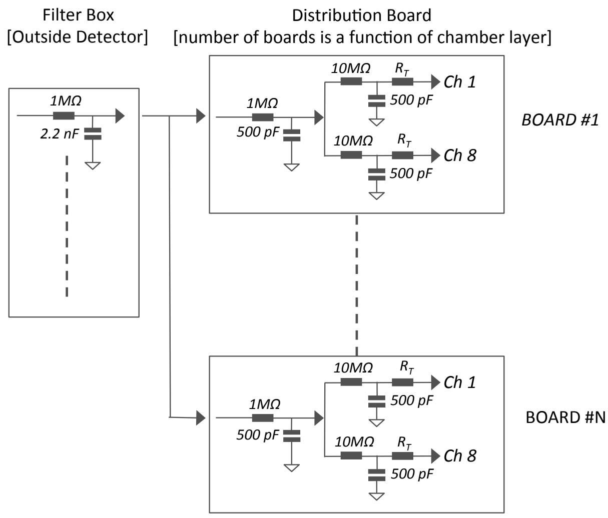

Figure 7.21: HV distribution network.

7.6 Gas system

The drift chamber is filled with a gas mixture of 90% helium and 10% isobutane. The gas system supplies the appropriate gas mixture to the chamber, while maintaining the required flow rate, pressure, purity, and composition stability. It includes safety items such as flammable gas sensors and release valves to protect the gas system, detector, and personnel from dangerous conditions caused by component failures or operator errors. To reduce the operating costs, 85% of the gas will be purified and recirculated.

The mixing will be done using mass flow controllers that will maintain the isobutane fraction at $(10.0 \pm 0.1)\%$. A parallel set of rotameters may be included to allow for high flow rate flushing. The system will allow a fraction of the flow to pass through a temperature-controlled water bath, which will be used if we decided to add water to help control the symptoms of aging.

The gas composition is verified using a set of analyzers to measure isobutane, oxygen, and water. The analyzer set will be able to sample gas at a variety of points in the gas system, such as before or after the gas enters the chamber or the filters.

This will be a recirculating gas system, which reduces operating costs and air pollution from the isobutane. The total flow will be 15 liters per minute, of which 2.5 liters per minute will be fresh gas. For a chamber volume of 5000 liters, this corresponds to four volume changes per day, or one volume of fresh gas every 1.5 days. The flow is controlled by an explosion-proof compressor, which is regulated to maintain a chamber pressure of 4.00 ± 0.05 mbar (0.4% of an atmosphere) above atmospheric pressure.

The primary gas lines between the gas mixing station and the detector will be welded and pressure-tested stainless pipe, 1.5 inches diameter. This will be reduced to 0.75 inch diameter in the cable trays through the detector. The input line is fanned out to 8 lines of 5 mm diameter on the rear endplate, while the output line is fanned out to 16 lines of 5 mm diameter on the forward endplate.

The gas returning from the detector passes through a palladium catalytic filter which removes oxygen by the reaction $13O_2 + 2C_4H_{10} \rightarrow 8CO_2 + 10H_2O$. The resulting water is removed by an alumino-silicate molecular sieve. The system contains two such sieves, so that one can be regenerated (i.e., have the absorbed water removed) by flushing with helium at elevated temperature without stopping operations. This filter system was originally built for the *BABAR* drift chamber and will be reused for SuperB.

The gas temperature and pressure will be monitored at various points in the system, along with atmospheric pressure. These quantities will be used to calculate gain correction due to gas density. We will also monitor gas gain using a small, single-cell chamber that will be mounted on the return line from the chamber. Any variations in the current induced by an ^{55}Fe source after applying the density correction would indicate gain variations due to gas composition or chamber aging.

The majority of the gas system components will be in the gas hut (or room), which will be located at an exterior wall of the interaction hall. Two additional racks close to the detector will contain bubblers, pressure sensors, and valves. The gas storage areas will be outside, under cover, immediately adjacent to the hut. The isobutane, since it is flammable, will be stored in a physically separate area from the other gases. The isobutane tanks and lines will be heated and insulated.

The gas system includes an extensive safety system to protect personnel and equipment. This system will be reviewed and approved by the laboratory. Aspects of the safety system include:

- ventilation in the gas hut, which, when combined with flow restrictors on the lines into the hut, ensure that a leak cannot create an asphyxiation hazard.
- nitrogen flows in the exhaust lines and into the electronics enclosures on both endplates.
- flammable gas sensors in the gas hut and the bubbler rack.

- an oxygen sensor on the return line.
- bubblers and redundant pressure sensors to protect the chamber against over pressure.
- an independent helium line and regulator to protect the chamber against sub-atmospheric pressures.
- administrative controls on changes to the gas system.

The system is designed such that it will remain safe even during extended power outages. We will undertake regular maintenance and keep sufficient spare parts to ensure reliable operations.

7.7 Calibration and monitoring - Roney 3 pages

7.7.0.1 Slow control systems

7.7.0.2 Calibration

7.7.0.3 Gas monitoring system

7.7.0.4 On-line monitor

7.8 Integration

7.8.1 Overall geometry and mechanical support

The envelope of the drift chamber is determined by the tungsten shield and the DIRC at the inner and outer radii, and by the backward calorimeter and the FTOF in the negative and positive z directions. There are 5 mm radial clearances between the drift chamber and the surrounding components, and 5 mm clearance between the drift chamber envelope and the backward calorimeter. The FTOF is directly mounted onto the drift chamber. The envelope in the backward direction includes the space occupied by the signal cables after they exit the enclosure.

In *BABAR*, the chamber was supported at the backward end by turnbuckles connecting the rear cylinder extension to the DIRC strong support tube. We envision using a similar system, although the actual mounting points used by *BABAR* will be obscured by the backward calorimeter.

In the forward direction, the drift chamber and FTOF form an integrated mechanical package, supported by the DIRC central support tube (CST). Figure. 7.22 shows the forwards mounting components used for the *BABAR* drift chamber. Note that the support point on the DIRC is on the z surface of the CST, not the inner radius. Because the Super*B* chamber is shorter in the forward direction than *BABAR*, the corresponding support tabs will be on the FTOF, not the chamber.

7.8.2 Installation and alignment

The chamber and FTOF will be installed prior to the forward and backward calorimeters and the tungsten shielding. The installation will reuse the existing *BABAR* equipment, which is currently stored at SLAC. The chamber is supported at the inner radius and slid along a supporting beam that passes through the inner cylinder (Fig. 7.23).

Both forward and backward enclosures will contain a number of precision 6 mm dowel into which target holders for corner-cube reflectors can be mounted. The enclosures in turn are doweled to precise reference holes on the endplates, referencing the target locations to the sense wire locations.

The mounting systems at both ends allow for several mm of adjustment in x and y. The chamber location will be adjusted to center the chamber in x and y on the interaction point and to align the sense wire direction with the magnetic field. The tolerances on these alignments have not yet been specified. The tolerance on the location in z will be significantly looser.

7.8.3 Services

The services required for the backward end are listed below. These will reach the backward enclosure via 16 slots in the outer radius of the steel plug located within the DIRC strong tube. Each slot will be approximately 50 mm in radius

Figure 7.22: Forward end mounting system on the *BABAR* drift chamber. (a) Tab on the outer radius of the drift chamber. (b) Corresponding mounting point on the CST.

by 250 mm wide. Cables continuing to the digitizing crates, located on the top of the detector, will be routed to wireways at the end of the IFR iron immediately after exiting the DIRC strong tube.

Note that within the radial extent of the backward calorimeter, the signal cables (and all other services) are routed to stay within the drift chamber envelope.

- Signal cables: approximately 8000 coaxial cables, RG-179, 2.54 mm in diameter, organized into 8-cable ribbons. These are 10 m in length, and travel to the digitizing electronics crates.

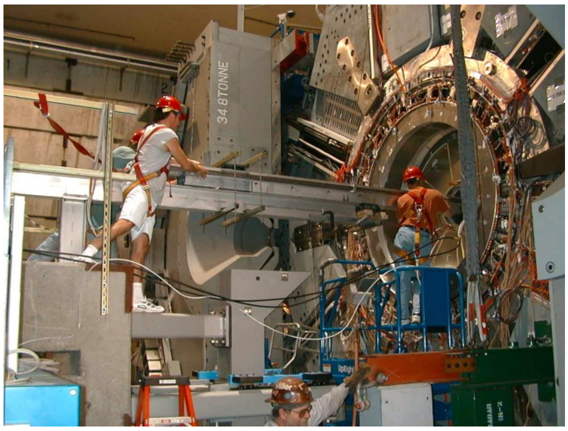

Figure 7.23: *BABAR* drift chamber during installation. The same tooling is available for use by Super*B*.

- Calibration cables: RG-179, one for every eight signal channels. Also originate at the digitizer crates.

- Low-voltage power: Four 1/0 welding cables, 14.7 mm diameter. Originate in the electronics hut.

- Cooling lines: 16 lines (8 separate circuits, each with a supply and a return line), 26.2 mm reinforced PVC. The sub-atmospheric water-based cooling system (Sec. 7.3.6) will be close to the detector, but outside of the radiation area.

- Drift gas: one line, 19 mm diameter stainless steel. Originates in the gas hut. This line increases to 38 mm diameter after exiting the detector.

- Nitrogen flush gas: two lines, 19 mm diameter stainless steel. Also from the gas hut.

The services for the forward end will exit the detector in the radial space between the tungsten shield and the FCAL. The services for the forward region are:

- High voltage: 16 56-conductor cables, 14 mm diameter. Originate at the HV supplies in the electronics hut.

- Drift gas: one line, 19 mm diameter stainless steel. Originates in the gas hut. This line increases to 38 mm diameter after exiting the detector.
- Nitrogen flush gas: two lines, 19 mm diameter stainless steel. From the gas hut.
- Cooling lines: 2 lines, 19 mm reinforced PVC. From the cooling system.

7.9 Bibliography

[1] R. Veenhof, *Garfield - simulation of gaseous detectors* CERN-W5050, Version 9.

[2] CLEO reference.

[3] M. Adinolfi *et al.* (KLOE Collaboration), *The tracking detector of the KLOE experiment*, Nucl. Instrum. Methods Phys. Res., Sect. A **488**, 51 (2002).

[4] M. Adinolfi *et al.* (KLOE Collaboration), *The tracking detector of the KLOE experiment*, Nucl. Instrum. Methods Phys. Res., Sect. A **488**, 51 (2002).

[5] A. Sharma, F. Sauli, Nucl. Instr. and Meth. A 350 (1994) 470.

[6] C. Avanzini et Al. Nuclear Instruments and Methods in Physics Research A449 (2000). 237-247.

[7] P.R.Burchat and John Hiser Studies of helium gas mixtures in drift chambers SLAC-PUB-5626 SCIPP 91/25 September 1991.